

TRANSITION ZONE WAVE PROPAGATION: CHARACTERIZING TRAVEL-TIME AND AMPLITUDE INFORMATION

Peter M. Shearer and Jesse F. Lawrence

University of California San Diego, Institute of Geophysics and Planetary Physics

Sponsored by Air Force Research Laboratory

Contract No. FA8718-06-C-0005

ABSTRACT

We characterize transition-zone seismic wave propagation by mapping and calibrating the travel-time and amplitude behavior of P waves traveling through the transition zone at epicentral distances from 13 to 30 degrees and modeling the triplications resulting from the 410- and 660-km discontinuities. We have built an online database of waveforms from the Incorporated Research Institutions for Seismology (IRIS) Fast Archive Recovery Method (FARM) archive from 1990 to 2005, which consists of broadband data from the global seismic networks as well as portable seismic arrays deployed in Program for Array Seismic Studies of the Continental Lithosphere (PASSCAL) experiments. We process the data in order to compute source and station amplitude terms to correct for different magnitude sources and near-receiver site effects as well as errors in the instrument response functions. We use records from the full teleseismic P distance interval to estimate source-time-function envelopes and deconvolve them from the traces, discarding data from sources that last longer than 60 s and signals with low signal-to-noise ratios ($\text{snr} < 3$). The deconvolved traces are stacked into bins according to distance, providing an initial distance (or Earth-structure) wavefield term. We also stack the deconvolved traces into bins for each station, providing an initial station wavefield term. Through several iterations we converge upon solutions for the event, station, and structure wavefield terms. This deconvolution technique is necessary to combine data from many different sources. We then compute both global and regional Earth-structure terms to obtain the average time-versus-distance amplitude of the wavefield, focusing on the 13 to 30 degree interval that is most sensitive to transition-zone structure. Because the timing of the secondary branches is quite variable, we implement an envelope-function stacking method in order to obtain robust results. We model our data stacks using WKBJ synthetic seismograms and a niching genetic algorithm to explore the model space of different transition-zone velocity structures. We compare these results with long-wavelength models of 410- and 660-km discontinuity topography obtained from SS precursors and more detailed images beneath individual seismic stations derived from receiver functions. Our goal is to produce integrated transition-zone models of seismic velocity and discontinuity topography that will improve our ability to locate and estimate magnitudes of events recorded at regional distances.

OBJECTIVES

This project studies the effects of heterogeneous transition-zone structure on seismic travel times and amplitudes. Accurate predictions of *P*- and *S*-wave travel times and amplitudes at distances between 13 and 30 degrees are hindered by the sensitivity of the multiple travel-time branches at these distances to variable structure in the mantle transition zone. Both discontinuity topography and bulk seismic velocity anomalies perturb seismic ray paths, which causes focusing and defocusing effects on wave amplitudes as well as travel-time anomalies. However, travel-time and amplitude information is critical for locating and estimating magnitudes of target events. By comparing regional variations of triplication amplitudes and travel times with predictions of 3D seismic velocity models, we will obtain improvements in mantle transition-zone models, as well as in the estimated locations and magnitudes of recorded events.

The effect of the mantle discontinuities at 410- and 660-km depth is shown in Figure 1, which depicts a series of *P*-wave ray paths between 13 and 35 degrees. Retrograde branches result from the velocity jump at each of the discontinuities, causing the familiar double triplication centered at about 20 degrees. However, the positions of these branches are very sensitive to the discontinuity depths, which typically vary by 30 km or more (e.g., Shearer, 1990, 1991, 1993; Shearer and Masters, 1992; Flanagan and Shearer, 1998a,b; Gu et al., 1998), and to the size of the velocity jumps at the discontinuities, which also exhibit considerable variation (e.g., Melbourne and Helmberger, 1998; Shearer and Flanagan, 1999; Chambers et al., 2005). In addition, there is some sensitivity to 3D velocity variations in the transition zone.

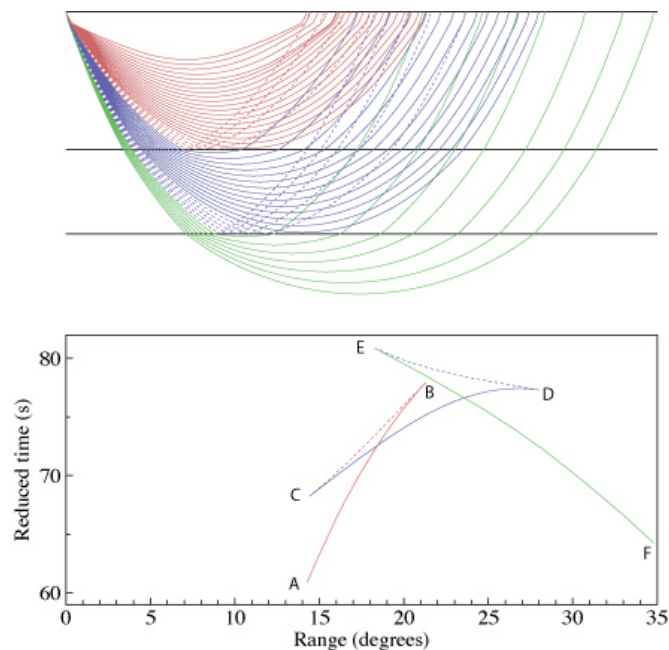


Figure 1. Discontinuities in the mantle transition zone at 410- and 660-km depths cause a pair of triplications in *P*- and *S*-wave arrivals between about 15 and 30 degrees. The ray paths (top) are color-coded, and correspond to the different branches in the travel-time curve plotted below (reduced at 10 s/degree). The AB branch consists of direct waves that bottom above the 410-km discontinuity (red solid). The BC branch reflects at 410 km (red dashed). The CD and DE branches bottom above and reflect off the 660-km discontinuity (blue solid and dashed). The EF branch bottoms in the lower mantle. This figure is adopted from Shearer (2000).

We compare observed *P*-wave travel times and amplitudes with predictions based on the best current models. These tests illuminate the strengths and weaknesses of these models, from which we determine if the models are sufficient to explain anomalous travel times and amplitudes at these distances (and consequently check to see how robust our current event locations and amplitude predictions are). This project compares times and amplitudes recorded at both temporary and permanent seismic stations for all triplication phases, not just the first arrivals. The triplications cause

difficulties for traditional methods of source location, magnitude estimation, and inversions for 3D velocity structure. Therefore, triplication data are typically avoided for seismic tomography and source location. However, details of the triplications can be useful for characterizing heterogeneity and calculating better source locations. With sufficient data the secondary branches can be used to model variations in discontinuity topography and seismic velocity. Once the structural properties are determined, the high sensitivity of triplication travel-time and amplitude fluctuations to source location and magnitude make triplications ideal for determining source characteristics. However, without an appropriate transition zone model, these times cannot yield accurate times or amplitudes.

The relevance of our results for nuclear test monitoring is that better structural models of transition-zone structure will reduce source location and magnitude uncertainties. The anomalous arrival times and amplitudes between 13 and 30 degrees currently limit the usefulness of regional phase data in calculating accurate source locations and event magnitudes. However, records from closer distances are not likely to be available in many parts of the world and small magnitude events are often not well recorded at longer distances because of the sharp drop in *P* and *S* amplitudes that occurs just beyond 30 degrees. Thus unraveling the complexities of the travel-time triplications and improving our models of the transition zone are likely to be critical for accurate monitoring of a significant number of target events.

RESEARCH ACCOMPLISHED

FARM Database

Our initial efforts have concentrated on assembling a database of waveforms from the IRIS FARM archive, which consists of broadband data from the global seismic networks as well as portable seismic arrays deployed in PASSCAL experiments. This involves transferring the data from the IRIS DMC and converting waveforms to seismic analysis code (SAC). We then run programs for quality assurance, redundancy checks, instrument response correction, meta-data archiving, and signal rotation to tangential and radial. The SAC files are currently stored on a RAID system, with backup for redundancy in the event of hardware failures.

We have also completed computing index files and signal-to-noise estimates for the *P* and *S* arrivals, which facilitates later processing and also provides a check on the timing integrity of the SAC waveforms. Our basic approach is to measure the signal-to-noise as the ratio between the maximum amplitude (peak to trough) in a time window that contains the phase of interest and a pre-event noise window of equal length. Because the raw data are broadband, we perform this operation separately for different frequency bands.

Amplitude Analysis

Triplicated phases are difficult to distinguish from each other, overlapping in time, and having varying amplitudes. This is further compounded by unconstrained source-time functions of the earthquake, and heterogeneous structure beneath seismic stations causing waveform variability. Here, we attempt to remove the source and station terms from all measured amplitudes for high signal-to-noise *P* waves, to constrain the amplitude variation that results from seismic structure. Initially we assume that the maximum peak-to-peak log amplitude (max-min), a_i , of the i^{th} *P*-wave is the sum of a source term, s_j , a receiver term, r_k , and an Earth response term, e_l ,

$$a_i = s_j + r_k + e_l. \quad (1)$$

Given N_d *P*-wave amplitudes, from any N_s sources, recorded at N_r sources, it is possible to solve for N_e Earth-response terms as a function of distance. The initial source term for each event is the mean of all a_i values for that event. The initial receiver terms are the means of all log amplitude measurements for that receiver minus the corresponding source terms ($r_k = a_i - s_j$). The distance-dependant Earth-response term is the mean of all log amplitude measurements for each distance minus the corresponding source and receiver terms ($e_l = a_i - s_j - r_k$). We can then iteratively solve for more accurate source, receiver, and Earth response terms, with

$$s_j = a_i - r_k - e_l \quad (2)$$

$$r_k = a_i - s_j - e_l \quad (3)$$

$$e_l = a_i - s_j - r_k. \quad (4)$$

When applied to all *P*-wave data in the FARM database, this method provides an estimate of amplitude as a function of distance, as shown in Figure 2. The overall amplitude versus distance behavior is very similar to that obtained by Veith and Clawson (1972) for magnitude calibration. The 13 to 33 degree distance range stands out as anomalous compared to the trend of decreasing amplitude with distance.

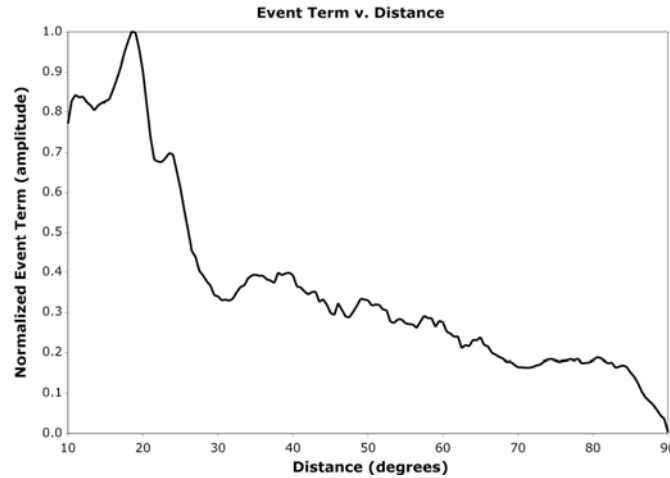


Figure 2. Distance-dependant Earth-response terms for amplitude from 10 to 90 degrees.

We have adapted a WKBJ synthetic seismogram code (Chapman, 1978) to generate suites of model predictions for comparisons to the data. Our analyses have concentrated on characterizing the globally averaged wavefield as a starting reference point for studies of regional variations. By comparing the Earth-response amplitude terms to WKBJ synthetic waveform amplitudes, it is possible to determine which seismic models are most probable. The amplitudes in the 13 to 33 degree range are sensitive to the seismic velocity structure of the transition zone. Amplitudes are highly sensitive to interface depth, sharpness, and velocity contrast for each of the discontinuities (410, 520, and 660). Figure 3 shows how amplitude can vary with small changes in seismic velocity structure. While not modeled here, the amplitudes are also strongly dependant upon quality factor, or attenuation, structure.

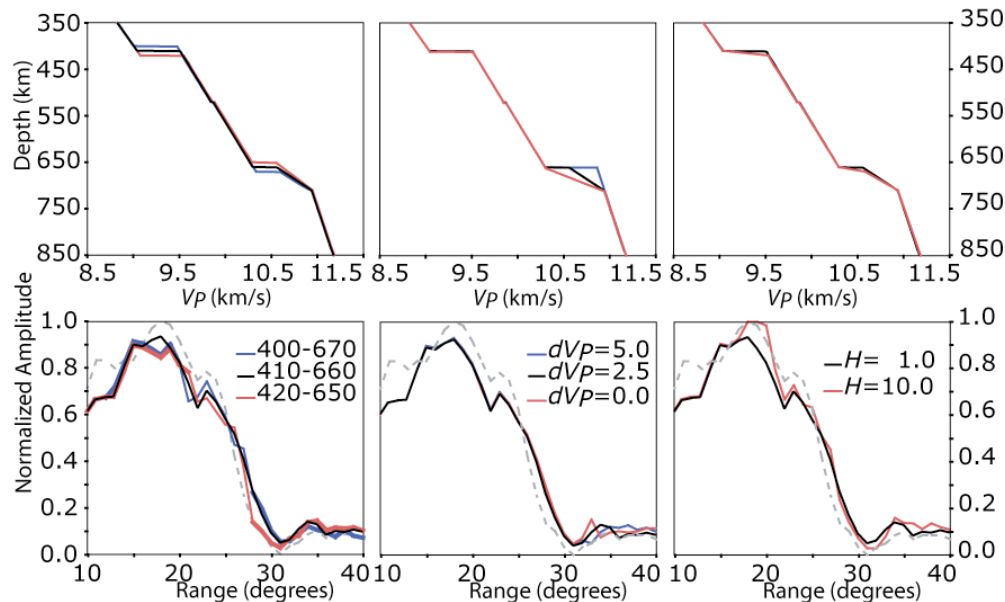


Figure 3. Examples of three different types of perturbations to transition zone structure: a) transition zone thickness, b) velocity contrast, and c) interface thickness. The corresponding WKBJ maximum amplitudes for *P* waves (d-f) change as a function of distance. The models are shown as black, blue, and red lines. The data are the dashed line.

Here, we model these data with a mass-forward modeling algorithm called the Niching Genetic Algorithm (NGA) (Koper et al., 1999). The NGA uses an evolutionary paradigm to create, mutate, and breed a population of velocity structure models such that those with poor fits to the data are eliminated, and those with good fits survive to continue the search of the model space for the best solution. Using this paradigm, we find the optimal solution to the *P*-wave data (Figure 4). This model is similar to the *P*-wave velocity structure found by Lawrence and Shearer (2006) using NGA waveform modeling of reflected energy from the transition zone (*PdP*, *SdS*, *Pds*, and *Pdpd*).

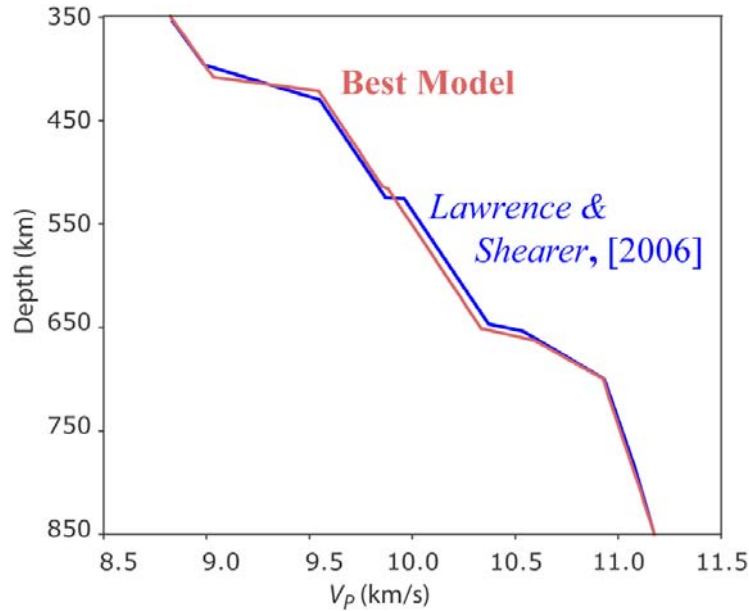


Figure 4. The (red) best fit model after 100 generations of an NGA simulated inversion yields a similar result to a similar parameter search based on (blue) *PdP*, *SdS*, *Pds*, and *Pdpd* reflected phases (Lawrence and Shearer, 2006).

Wavefield Analysis

In the amplitude section, we neglected time other than to ensure that we have windowed the appropriate phase. Here, we introduce a similar analysis that iteratively solves for time-dependent source, station, and Earth-response terms. Mathematically, one can conceptualize a waveform, $a(t)$, as the convolution of the source term, $s(t)$, the receiver term, $r(t)$, and the distance-dependant Earth-response term, $e(\Delta, t)$, plus noise, $n(t)$,

$$a(t) = s(t) * r(t) * e(\Delta, t) + n(t). \quad (5)$$

Here, we assume that the source term, s , is a combination of the earthquake rupture and the near-source Earth response function. Furthermore, the receiver term is idealized as the convolution of the instrument response and the near-receiver Earth response.

Ideally, one could estimate the deep-Earth response by stacking waveforms with the source and receiver terms ($s(t)$ and $r(t)$) deconvolved. Unfortunately, the source and receiver terms are poorly constrained, the waveforms are not easily stackable because of dissimilarity and polarity issues, and noise is typically problematic. Therefore we develop and employ an automated stepwise stacking and deconvolution technique to boost the signal-to-noise ratio and to solve for the time-dependant source and receiver terms. We improve waveform similarity by examining the instantaneous amplitude or envelope function of the wavefield, $a_E(t)$, rather than the raw waveform. We initially estimate the source, receiver, and Earth-response functions as delta functions with amplitudes provided by the amplitude analysis above.

With preliminary estimates of s , r , and e , we can iteratively solve for each term from the envelope function,

$$\begin{aligned}
 s(t) &= a_E(t)^{*^{-1}} r(t)^{*^{-1}} e(\Delta, t) \\
 r(t) &= a_E(t)^{*^{-1}} s(t)^{*^{-1}} e(\Delta, t). \\
 e(\Delta, t) &= a_E(t)^{*^{-1}} s(t)^{*^{-1}} r(t)
 \end{aligned}
 \tag{6}$$

With this analysis, we obtain a time- and distance-dependant Earth-response term. For all data in the FARM database, the Earth-response term is shown in Figure 5.

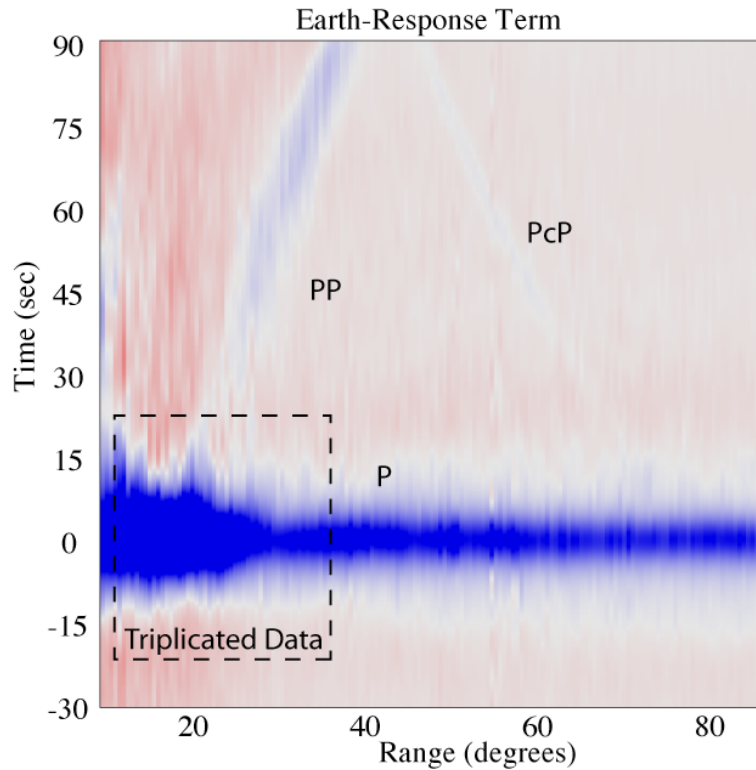


Figure 5. The time- and distance-dependant Earth-response function calculated from all FARM *P*-wave data. The box outlines the region of tripllicated data. Blue is positive amplitude, red is negative. Various phases are indicated as *P*, *PP*, and *PcP*.

We can calculate synthetic time- and distance-dependant Earth-response functions using WKBJ. To estimate the appropriate frequency content and heterogeneity, we deconvolve the *P*-wave slant-stacked synthetic waveforms from 45 to 80 degrees and convolve the stacked observed waveforms for the same distance range. Synthetics using the model of Lawrence and Shearer, (2006) (LS06) are similar, but not identical to the observed Earth-response functions (Figure 6.a). Variants from LS06 demonstrate how the Earth-response function changes as a result of structure (Figure 6.b-d).

The optimal *P*-wave model found with a niching genetic algorithm simulated inversion for the wavefield is remarkably similar to the most optimal model found in Figure 4. Note that the most optimal model is merely representative as we assume that 3D heterogeneity has a broadening effect, and that we do not know precisely the scale of this heterogeneity. The primary difference between the optimal model found with wavefield analysis and that from amplitude analysis, is that the estimated depths for the global model are slightly different, which accounts for the timing. Recall that timing is inherently included in the wavefield analysis and not in the amplitude analysis. We expect that this method will also work with shear waves, although so far we have only examined *P* waves.

Once the station terms are well defined with the global analysis, it is possible to perform regional amplitude or wavefield analysis for high-quality individual events or sets of events. With less data it is critical to use only high-quality events and well-calibrated stations.

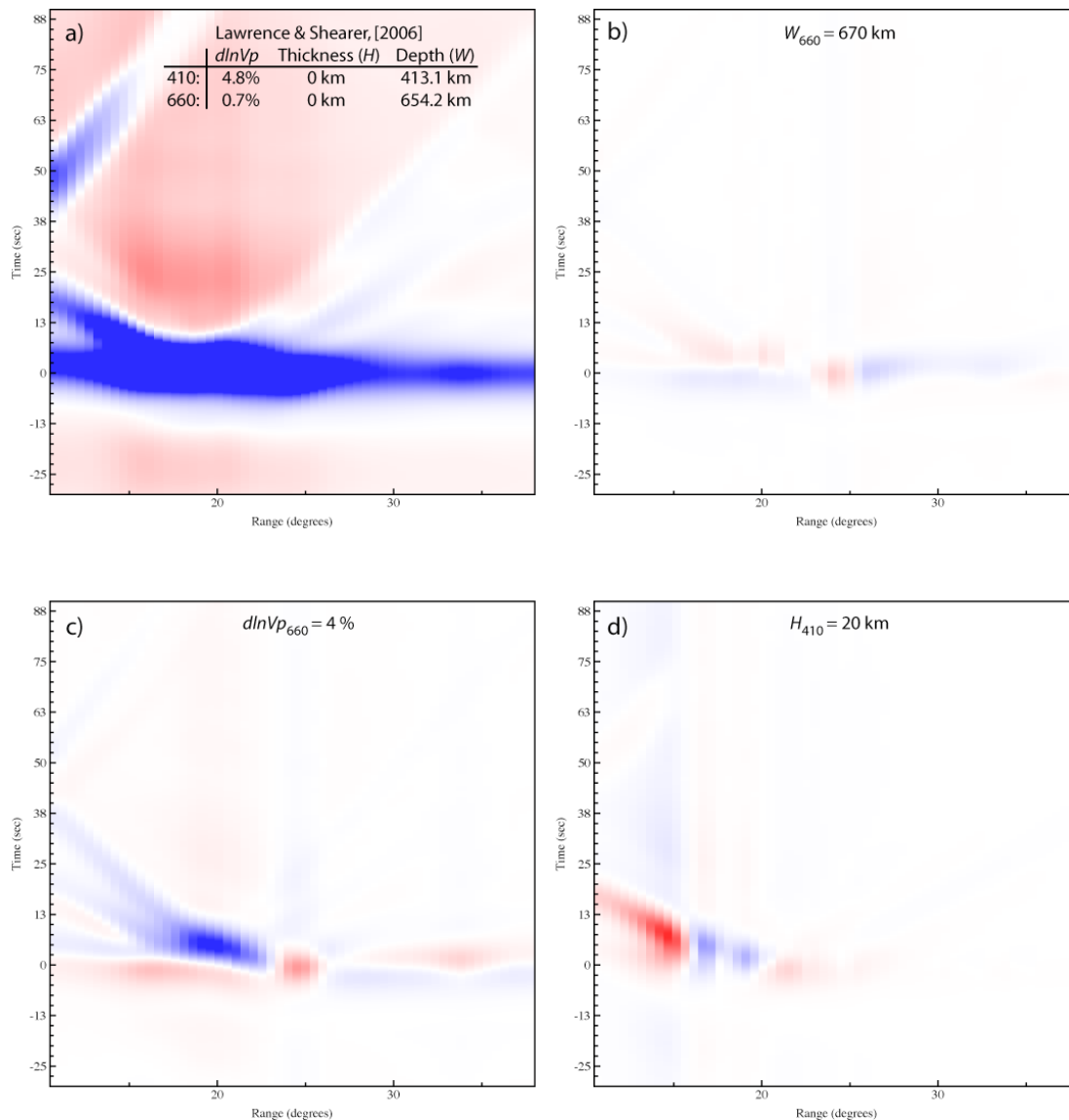


Figure 6. This figure shows a) the synthetic Earth-response function for the seismic velocity model found by Lawrence and Shearer (2006) (LS06), and deviations in Earth-response functions relative to LS06 as a result of b) a deeper 660 interface, c) a larger V_{p660} contrast, and d) a thick 410 interface. Blue is positive, red is negative.

CONCLUSIONS AND RECOMMENDATIONS

This analysis has shown that it is possible to divide amplitude terms from digital seismic records into source, receiver, and Earth-response terms that account for the complicated wavefield variations in the 13 and 33 degree distance range. Through a multi-dimensional component analysis, each term is obtained iteratively. With well-resolved receiver terms and Earth-structure, it may be possible to estimate source functions with data at these regional distances. Note that the method requires large numbers of seismograms from many stations with data to achieve reliable results. It is only in the past few years that global data and station coverage have increased to a sufficient level that such an analysis can be roughly conducted. In the future, improved results are likely as more data are collected from regions of increased station coverage.

ACKNOWLEDGEMENTS

The data used here were supplied by IRIS DMC. We thank Kris Walker for his efforts with the FARM database.

REFERENCES

- Chambers, K., A. Deuss and J.H. Woodhouse (2005). Reflectivity of the 410-km discontinuity from PP and SS precursors, *J. Geophys. Res.* 110: B02301, doi:10.1029/2004JB003345.
- Chapman, C. H., (1978) A new method for computing synthetic seismograms, *Geophys. J. Astro. Soc.* 54: 481–518.
- Flanagan, M.P. and P.M. Shearer (1998a). Global mapping of topography on transition zone velocity discontinuities by stacking SS precursors, *J. Geophys Res.* 102: 2673–2692.
- Flanagan, M.P. and P.M. Shearer (1998b). Topography on the 410-km seismic velocity discontinuity near subduction zones from stacking of sS, sP, and pP precursors, *J. Geophys. Res.* 103: 21,165–21,182.
- Gu, Y., A.M. Dziewonski and C.B. Agee (1998). Global decorrelation of the topography of transition zone discontinuities, *Earth Planet. Sci. Lett.* 157: 57–76.
- Koper, D. K., M. E. Wysession, and D. A. Wiens (1999). Multimodal function optimization with a niching genetic algorithm: a seismological example, *Bull. Seism. Soc. Am.* 89: 978–988.
- Lawrence, J.F., and P.M. Shearer (2006). Constraining seismic velocity and density for the mantle transition zone with reflected and transmitted waveforms, G^3 , doi:10.1029/2006/GC001339.
- Melbourne, T. and D. Helmberger (1998). Fine structure of the 410-km discontinuity, *J. Geophys. Res.* 103: 10,091–10,102.
- Shearer, P.M. (1990). Seismic imaging of upper-mantle structure with new evidence for a 520-km discontinuity, *Nature*, 344, 121–126.
- Shearer, P.M. (1991). Constraints on upper-mantle discontinuities from observations of long-period reflected and converted phases, *J. Geophys. Res.*, 96, 18147–18182.
- Shearer, P.M. (1993). Global mapping of upper mantle reflectors from long-period SS precursors, *Geophys. J. Int.*, 115, 878–904.
- Shearer, P.M. (2000). Upper mantle seismic discontinuities, in *Earth's Deep Interior: Mineral Physics and Tomography from the Atomic to the Global Scale*, AGU Geophysical Monograph 117: 115–131.
- Shearer, P.M. and M.P. Flanagan (1999). Seismic velocity and density jumps across the 410- and 660-kilometer discontinuities, *Science* 285: 1545–1548.
- Shearer, P.M. and T.G. Masters (1992). Global mapping of topography on the 660 km discontinuity, *Nature* 355: 791–796.
- Veith, K.F. and G.E. Clawson (1972). Magnitude from short-period P-wave data, *Bull. Seismol. Soc. Am.* 62: 435–452.